### Title

Development and Application of a Coarse-Grained Model for PNIPAM by Iterative Boltzmann Inversion and Its Combination with Lattice Boltzmann Hydrodynamics




### Journal

The Journal of Physical Chemistry B, 121(45)

### ISSN

1520-6106



### Authors

Boţan, Vitalie
Ustach, Vincent D
Leonhard, Kai
et al.



### Publication Date

2017-11-16

### DOI

10.1021/acs.jpcb.7b07818

Peer reviewed

# Development and Application of a Coarse–Grained Model for PNIPAM by Iterative Boltzmann Inversion and its Combination with Lattice Boltzmann Hydrodynamics

Vitalie Boţan,[†,¶] Vincent D. Ustach,[‡,¶] Kai Leonhard,[*,†] and Roland Faller[*,‡]

†*Lehrstuhl für technische Thermodynamik, RWTH Aachen University, Schinkelstr. 8, 52062 Aachen, Germany*

‡*Department of Chemical Engineering, University of California–Davis, Davis, CA, 95616*

¶*These authors contributed equally.*

E-mail: kai.leonhard@ltt.rwth-aachen.de; rfaller@ucdavis.edu

Phone: +1 530 752-5839. Fax: +1 530 752-1031

**Abstract**

The polymer (PNIPAM) is studied using a novel combination of multiscale modeling methodologies. We develop an iterative Boltzmann inversion potential of concentrated PNIPAM solutions and combine it with Lattice Boltzmann as a Navier Stokes equation solver for the solvent. We study in detail the influence of the methodology on statics and dynamics of the system. The combination is successful and significantly simpler and faster than other mapping techniques for polymer solution while keeping the correct hydrodynamics. The model can semi–quantitatively describe the correct phase behavior and polymer dynamics.

# Introduction

Poly(N–isopropylacrylamide) (PNIPAM) is an important technical polymer. It is a responsive/active polymer as it changes conformation under controlled changes of the environment. It is used e.g. in microgels, sensors, tissue engineering, and drug delivery.[1–3] Its conformation, particularly in brushes, can be controlled by external stimuli and therefore it can be considered a switchable material.[4] The switching depends on its solubility in water and other solvents. Stimuli–sensitive hydrogels offer great potential as targeted drug delivery vehicles. In particular, temperature sensitive hydrogels with a well–defined volume phase transition exhibit expansion or shrinkage.[5]

PNIPAM shows interesting, complex phase and conformation behavior as function of temperature, solvent composition, ion concentrations and pH. It has a lower critical solution temperature/volume phase transition temperature (LCST/VTPP) and exhibits co–nonsolvency where it is soluble in a range of pure solvents (water, alcohols) but not in all concentrations of their mixtures.[6]

Simulations can resolve some of the underlying characteristics for these behaviors as they obtain molecular–level information complementary to experiments. However, no single simulation model to date can describe the full complexity of PNIPAM. Particularly, length

scales from one atom to several 10s of nm and time scales from sub–fs to several $\mu$s[7] would have to be covered within such a model. Consequently, the majority of computational studies of PNIPAM solutions over the last two decades has addressed – with few exceptions[8–10] – its single–chain behavior in the infinite dilution limit.[11–15] A remarkable diversity in force–fields (FFs), ranging from the generic Dreiding FF[16] through organic and biomolecular FFs such as OPLS,[17,18] GROMOS,[19,20] and AMBER[21] to the polymer consistent FF (PCFF)[22] has been employed. These FFs were used to study effects of chain length,[23] stereotacticity[24–26] and/or hydration properties,[27,28] but only recently it was recognised that due to slow relaxation dynamics of single–chain conformations especially at low temperatures considerably longer simulations than 100 ns are required[29] for accessing equilibrium behavior of even single PNIPAM chains. Moreover, in a very recent study[7] it was shown "that the simulation duration of 1 $\mu$s is not long enough to provide meaningful information on the equilibrium behavior of a PNIPAM chain, and the transition temperatures mentioned should not be taken as a thermodynamic transition temperature for PNIPAM". Thus, the time and length scales are too large for atomistic simulation and coarse graining is required. However, due to the strong temperature and composition dependence the development of an effective potential based on established CG methodology is challenging. Up to date there are only two reports on construction of a systematic CG model of PNIPAM,[30,31] and they both focus on a single–chain model in the infinite dilution limit. In this study we present the first development of a systematic CG model of PNIPAM solutions at finite concentrations.

The main idea behind any coarse–graining scheme is to obtain an effective mesoscale interaction potential that accurately describes the structural, thermodynamic and/or dynamical properties of the underlying atomistic system, albeit matching all of them is scarcely possible. The iterative Boltzmann inversion (IBI) is a fairly simple and generic structure–based coarse–graining method:[32] it derives a coarse–grained model from radial distribution functions (RDF) as well as bond length and angle distributions of an atomistic system. One calculates the structural descriptors (e.g. RDF) of pre–selected mapping points from (typ-

ically) atomistic monomers which serve as mesoscale interaction centers. In the first step, a non–bonded interaction potential is produced by "Boltzmann–inverting" the RDF, i.e., a potential energy is approximated by a free energy. However, the direct inversion is only useful for obtaining a starting potential for the iterative approach and no direct physical meaning can be assigned to it. After the first mesoscale simulation the difference between the simulated and the target RDF is determined. A Boltzmann inversion of this difference leads to a correction to the potential. This is iterated until the difference between the target structure and the structure in the CG model is below a predefined tolerance. In systems with multiple mapping site types we sort the interaction between the components (e.g., A and B) into two categories, the A–A and B–B interaction of molecules/interaction centers with the same chemistry and the A–B interaction between different types. Since the self–interaction in e.g. a blend is not the same as in the melt and no mixing rules can be a priori assumed[33] there are three independent target functions for a binary system and correspondingly more for higher mixtures.[34] However, CG potentials based on consistency with respect to the structural and/or thermodynamic properties of underlying atomistic model do not guarantee the accuracy of the resulting dynamic behavior. Although IBI is typically performed for melts,[35] it has also been used to study polymer–solvent systems such as poly(acrylic acid) in water[36] and poly(isoprene) in toluene.[37]

Dynamic properties like diffusion or time correlations, are not necessarily recovered from a simple molecular dynamics simulation with such CG potentials. This is due to the fact that coarse–graining necessarily eliminates degrees of freedom that should appear in the coarse–grained dynamics in the form of dissipation and thermal noise. To address this problem different approaches have been explored, such as Lattice–Boltzmann methods,[38] dissipative particle dynamics,[39–41] multi–particle–collision (or stochastic rotational) dynamics,[42] and Stokesian dynamics.[43]

The Lattice–Boltzmann (LB) technique is an efficient way to describe a fluid obeying the Navier–Stokes equation.[38] It does not represent explicit solvent particles, but rather local

particle densities with mass and momentum. In LB the fluid exists as density packets on a three dimensional square grid of nodes *aka* the lattice. The fluid follows a two–step scheme: the streaming step followed by the collision step. In the streaming step, fluid moves to neighboring nodes along discrete velocity links. In the collision step, inbound fluid densities at every node exchange momentum and relax towards an equilibrium that represents the Maxwell–Boltzmann velocity distribution. For a thorough explanation and demonstration of the capabilities of LB, see e.g. Dünweg and Ladd.[38] Compared to full MD of explicit solvents, LB is computationally highly efficient. It is inherently parallelizable due to the grid representation of fluid populations, and a dramatic improvement in speed can be achieved using GPU processing[44] which is especially suited to mesh systems like LB.

For polymer solutions the correct momentum transport through the solvent is important to correctly represent the dynamics. Particularly at low to intermediate concentrations, most of the system consists of largely uninteresting solvent molecules. It therefore is advantageous to use a Navier-Stokes equation solver for the solvent and combine it with MD. LB was first joined with MD in 1999 by Ahlrichs and Dünweg[45] by coupling the fluid to the individual monomers of a polymer chain. The force of the fluid is imposed upon the MD beads using a modified Langevin equation. All polymer applications of LB with MD have focused on simple polymer models[45–47] where we cannot expect a direct experimental correlation of the results except for simple scaling results.

Combining systematically coarse–grained MD with LB has never been attempted. Particularly, the transfer of a coarse–grained potential between different integrators (MD and LB–MD) has not yet been studied. In this paper we combine for the first time a systematically coarse–grained potential based on the IBI technique with Lattice Boltzmann hydrodynamics.

We are using the modified Langevin equation approach as introduced by Ahlrichs and Dünweg[45]

$$\overline{F}_{fl} = -\xi_{bead}\left[\overline{v} - \overline{u}(\overline{r}, t)\right] + \overline{f}_s, \tag{1}$$

where $\overline{F}_{fl}$ is the force between polymer and fluid at a given point, $\xi_{bead}$ the resistance factor, $\overline{v}$ the particle velocity, $\overline{u}(\overline{r}, t)$ the fluid velocity interpolated at the given position $\overline{r}$ between the nearest grid points, and $\overline{f}_s$ a noise term that follows the fluctuation dissipation theorem. The bead resistance $\xi_{bead}$ is a tunable parameter corresponding to the local friction. Finite concentration systems have been successfully coupled to LB, including semidilute polymer systems[48] and spheres with 45 % by volume.[49]

# Methods and Models

## Atomistic simulations as target for mapping

Atomistic MD simulations have been performed with the LAMMPS simulation package[50] and its GPU–acceleration.[51] We have employed the AMBER 94 force field[21] for ONIPAM (oligomers) and the rigid SPC/E model for water[52] for the atomistic parent simulation. In previous work with the original AMBER 94 force field parameters and 2 different rigid water models (TIP3P and SPC/E), the LCST temperature for NIPAM trimers was too low[29] and we could not reproduce the phase behavior of the polymer–water solution in the temperature range of experimental interest. Very recently[10] this behavior was confirmed for isotactic NIPAM 30–mers with AMBER 94 forcefield and SPC/E water model. To overcome the unfavorably strong aggregation of oligomers, which prevents polymer solvation below the experimental critical temperature of 305 K (this value was determined for high molecular weight PNIPAM solution, for short oligomers a higher value is anticipated, depending on chain length and tacticity[26,53]), the Lennard–Jones well depth $\varepsilon$ has been scaled by a factor 1.35 for all interactions of the polymer carbons and hydrogens with water oxygen, and hence it solubilized the polymer backbone and isopropyl groups below the LCST, but still kept

them insoluble above the LCST.

The charges of the atomistic trimer have been computed at the B3LYP/TZVP level using the PCM solvation model, $\epsilon = 4$, and the RESP method as suggested by[54] Since the 3 monomers in the trimer are not chemically equivalent, they do not have a charge of exactly 0 but their charges are between $-0.1$ and 0.1 elementary charges. For the decamer, the charges of the middle monomer of the trimer have been manually adjusted to a total charge of zero since a full QM calculation of the decamer was deemed unnecessary and the small adjustments were estimated to have no appreciable effect on the individual interactions. The full model is available in supplementary information.

This paper focuses on the comparison of the all–atom (AA) and coarse–grained (CG) force–fields. The details of the atomistic force field calibration based on the experimental LCST data of short oligomers will be published elsewhere.

In the atomistic model with explicit water under experimental conditions the local structure properties highly depend on polymer concentration and cannot be captured in single–chain simulations in the infinite dilution limit. Therefore, we have chosen 24 atactic chains where we use three different realizations of tacticity: *m*–*m*–*r*–*m*–*r*–*r*–*m*–*r*, *m*–*r*–*r*–*m*–*m*–*r*-*r*–*r*, *r*–*r*–*r*–*m*–*m*–*r*–*r*–*r*, and each realization is used eight times. All chains have the same length $N_p = 10$ solvated in water for a set of concentrations and temperatures below and above the LCST. Due to the computational workload the polymer length is chosen to be as small as possible, but still about the PNIPAM persistence length,[55] besides that it is the shortest experimentally controllable degree of polymerisation. Both AA and CG are the same lengths for direct comparison. In Table 1 we present our system parameters for all–atom and coarse–grained models. All simulations use periodic boundary conditions in all dimensions. The initial configuration was prepared in Packmol[56] starting from randomly placed polymer and water molecules at low density and subsequently equilibrated at constant ambient pressure and constant $T = 305$ K using the Nose–Hoover thermostat and barostat with damping relaxation times of 100 and 500 fs, respectively. The particle–particle particle–mesh

**Table 1: System sizes for the simulations performed in this study. $x_{w,o}$ is the polymer concentration used during the optimization of the potential in %wt, $x_{w,s}$ is the actual polymer concentration in the simulation in %wt, $T$ is the system temperature in K, $N_O$ is the total number of oligomers, $N_w$ is the number of water molecules, $L_B$ is the linear box size in $nm$, $dt$ is the MD time step in fs, $\xi$ is the LB input friction $\times 10^{-11}$ kg/s.**

| | Model | $x_{w,o}$ | $x_{w,s}$ | $T$ | $N_O$ | $N_w$ | $L_B$ | $dt$ | $\xi$ |
|---|---|---|---|---|---|---|---|---|---|
| 1 | AA–MD | – | 44 | 305 | 24 | 1920 | 4.6 | 2.0 | – |
| 2 | AA–MD | – | 44 | 290 | 24 | 1920 | 4.6 | 2.0 | – |
| 3 | AA–MD | – | 44 | 320 | 24 | 1920 | 4.6 | 2.0 | – |
| 4 | AA–MD | – | 33.5 | 305 | 24 | 3000 | 5.1 | 2.0 | – |
| 5 | AA–MD | – | 67.7 | 305 | 24 | 720 | 4.0 | 2.0 | – |
| 6 | AA–MD | – | 67.7 | 290 | 24 | 720 | 4.0 | 2.0 | – |
| 7 | AA–MD | – | 67.7 | 320 | 24 | 720 | 4.0 | 2.0 | – |
| 8 | CG–MD | 44 | 44 | 305 | 192 | – | 9.2 | 2.0 | – |
| 9 | CG–MD | 44 | 44 | 290 | 192 | – | 9.2 | 2.0 | – |
| 10 | CG–MD | 44 | 44 | 320 | 192 | – | 9.2 | 2.0 | – |
| 11 | CG–MD | 67.7 | 67.7 | 305 | 192 | – | 8.0 | 2.0 | – |
| 12 | CG–MD | 67.7 | 67.7 | 290 | 192 | – | 8.0 | 2.0 | – |
| 13 | CG–MD | 67.7 | 67.7 | 320 | 192 | – | 8.0 | 2.0 | – |
| 14 | CG–LB | 44 | 44 | 305 | 192 | – | 9.33 | 18.9 | 1.683 |
| 15 | CG–LB | 44 | 44 | 305 | 192 | – | 9.33 | 18.9 | 22.44 |
| 16 | CG–LB | 44 | 44 | 305 | 192 | – | 9.33 | 189 | 1.683 |
| 17 | CG–LB | 44 | 44 | 290 | 192 | – | 9.33 | 18.9 | 1.683 |
| 18 | CG–LB | 44 | 44 | 320 | 192 | – | 9.33 | 18.9 | 1.683 |
| 19 | CG–LB | 44 | 67.7 | 305 | 192 | – | 8.0 | 18.9 | 1.683 |
| 20 | CG–LB | 44 | 33.5 | 305 | 192 | – | 10.33 | 18.9 | 1.683 |
| 21 | CG–LB | 67.7 | 67.7 | 305 | 192 | – | 8.0 | 18.9 | 1.683 |
| 22 | CG–LB | 67.7 | 67.7 | 305 | 192 | – | 8.0 | 18.9 | 22.44 |
| 23 | CG–LB | 67.7 | 67.7 | 305 | 192 | – | 8.0 | 189 | 1.683 |
| 24 | CG–LB | 67.7 | 67.7 | 290 | 192 | – | 8.0 | 18.9 | 1.683 |
| 25 | CG–LB | 67.7 | 67.7 | 320 | 192 | – | 8.0 | 18.9 | 1.683 |

(PPPM) method[57] with a real–space cutoff of 1 nm was used for evaluating the electrostatic interactions with an RMS accuracy of $10^{-4}$. The SHAKE algorithm[58] constrains water bondlengths and angles, so that a time step of 2 fs could be employed. After equilibration for at least 1 ns, the thermostat was set to a temperature according to Table 1 followed by a production run for 50 . . . 600 ns, during which several distribution functions and the time evolution of polymer end–to–end vectors and middle monomer center–of–mass displacement were analyzed.

## Iterative Boltzmann Inversion to generate a CG simulation model

Construction of a reliable CG model that successfully retains the structure of the underlying atomistic model is challenging: the quality of the CG model depends on how well the effective pairwise additive potential approximates the interplay of potential based interaction and packing, it is therefore crucial to appropriately define interaction sites between mesoscale structural units. These interaction sites are modeled as CG beads, and each individual CG bead represents a group of several atoms and is typically described via mapping functions, which determine the CG coordinates of each site as a linear combination of coordinates for the involved atoms. Our mapping for the NIPAM chains uses two beads per monomer: a backbone bead B and a side–chain bead A, with the structural units of $-CH_2CH-C{=}O-$ and $-NH-C_3H_7$, respectively. The interaction centers are the centers of mass of the involved atoms. This mapping scheme retains the local structural environment and can in principle preserve chain tacticity, if appropriate dihedral interactions keep the side–chain beads from flipping across the backbone, though in our implementation tacticity is not preserved as we did not use CG dihedrals. We did not distinguish between *meso* and *racemo* dyads in the analysis of dihedral A–B–B–A and B–B–B–B structures, which may have resulted in the weakly pronounced dihedral structures. Due to differences in size and mass due to an additional hydrogen in the end $-CH_3$ group as well as general end effects, all contributions from terminal B beads were neglected in derivation of the CG potentials. The resulting CG

model represents atactic NIPAM decamers consisting of 192 atoms as a 20 bead atactic chain (Figure 1).

We decompose the total potential energy in the CG model $U_{tot}^{CG}$ into bonded $U_{bond}^{CG}$ and non–bonded $U_{nb}^{CG}$ contributions

$$U_{tot}^{CG} = \sum U_{bond}^{CG} + \sum U_{nb}^{CG}. \tag{2}$$

$U_{bond}^{CG}$ is treated as a sum of independent bond stretching and angle bending potentials. The three types of CG potentials used in this work are as follows: (1) the bond stretching potentials, $U_{BB}^{CG}$ and $U_{AB}^{CG}$, between neighboring CG beads, (2) the angle bending potentials, $U_{BBB}^{CG}$ and $U_{ABB}^{CG}$, (3) the non–bonded interaction potential, $U_{nb}^{CG}$, between beads on different chains or between beads on the same chain, separated by at least 3 contiguous beads. Following the idea of the Boltzmann inversion (BI) method,[59,60] we assume here that bonded degrees of freedom (DOF) are approximated as independent, so that they obey independent Boltzmann distributions in the canonical ensemble:

$$P^{CG}(q) = Z^{-1} \exp\left[-U_{bond}^{CG}(q)/k_B T\right], \tag{3}$$

where $Z$ is a partition function, which acts as a normalization factor and $P^{CG}$ is a distribution function of the CG DOF. The bonded CG potential is obtained as the potential of mean force (PMF) by inverting Eq.3 and sampling corresponding distribution functions $P^{CG}$ (histograms, normalized by the appropriate Jacobian – $r^2$ for bond stretching and $\sin\theta$ for angle bending) from atomistic simulations of polymer–water solutions at 305 K. The dihedrals between four consecutively bonded CG beads revealed no specific features and were not considered. The BI method has several issues: the validity of the assumptions strongly depends on the chosen mapping scheme and has to be shown for each scheme. If bonded DOF are not independent, $U_{bond}^{CG}$ has to be refined iteratively to match reference atomistic distributions and/or CG bonds become interdependent. The derived potential has an ex-

plicit temperature dependence and its applicability is generally limited to the close vicinity of the reference temperature. Lastly, poorly sampled regions of phase space (e.g. high potential barriers) require either potential extrapolation with possibly undesirable artifacts or advanced sampling methods.

The IBI method is a natural extension of the BI method, as it aims to derive a non–bonded pair interaction potential $U_{nb}^{CG}$, which reproduces the target RDF $g_{ref}(r)$ from reference atomistic simulations. In the infinite dilution limit, the pair interaction potential can be obtained by using the PMF

$$U_{nb}^{0} = -k_B T \ln g_{ref}(r). \tag{4}$$

For finite concentrations the direct inversion PMF potential is not accurate enough due to many–body contributions, i.e. mainly packing effects, and needs to be refined iteratively:[32]

$$U_{nb}^{i+1} = U_{nb}^{i} + \alpha k_B T \ln \left[ \frac{g_i(r)}{g_{ref}(r)} \right]. \tag{5}$$

Here, $g_i(r)$ is the RDF obtained from a CG simulation with the $U_{nb}^{i}$ potential, and $\alpha = 0.7$ is a mixing parameter, introduced to smear out numerical instabilities. The iterative procedure is initiated with the PMF from Eq. 4, and the correction to the potential is made in each iteration step by assuming one–to–one correspondence between the potential at a given distance and the value of the RDF at the same distance. The box size was set to the average value of the periodic cell size of the reference atomistic system and RDF sampling was performed in the canonical ensemble using the same number of NIPAM oligomers and temperature as in the parent atomistic simulation. The iterative process ends when the ratio of RDFs between the reference and current models is close to one, i.e., when the CG structure has converged to the atomistic one. The degree of convergence can be quantified by evaluating the following $L_2$–error function:

$$f_i = \int \left( g_i(r) - g_{ref}(r) \right)^2 \mathrm{d}r, \tag{6}$$

and requiring the relative error to be within 1–5 %. The error function defined in Eq. 6 is a function of concentration and potential type: the optimized A–A potential has in the end the smallest relative error at both concentrations – 0.97 % at 67.7 %wt and 1.1 % at 44 %wt. The A–B potential converged to within 2.9 % and 3.2 % at 67.7 %wt and 44 %wt, respectively. The B–B potential has the largest tolerance: 3.7 % at 67.7 %wt and 7.1 % at 44 %wt.

The original IBI method is best suited for systems with uniform density. For two–component system with one component dissolved in another, the derived potential with implicitly included solvent DOF strongly depends on the simulation conditions, such as solute concentration, temperature and pressure, at which it has been developed. We have included the IBI tabulated potentials in the SI at the 44 %wt and 67.7 %wt state points. To investigate the transferability of the developed CG potential, we follow the strategy proposed in the author's previous work[61] and compare the CG structural and dynamical properties at different temperatures and concentrations with the atomistic reference calculations.

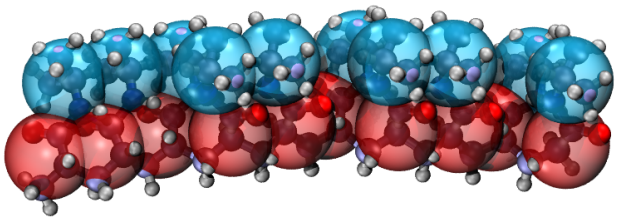

Figure 1: Mapping scheme for NIPAM decamer. Blue transparent spheres represent side beads A consisting of the $-NH-C_3H_7$ group of atoms and the red transparent spheres show backbone beads B consisting of $-CH_2CH-C=O-$ structural units.

AA–MD and CG–MD optimization simulations (without LB) for the IBI procedure were performed using the LAMMPS simulation package[50] with GPU accelerated styles for non-bonded potentials.[51] The Versatile Object–Oriented Toolkit for Coarse–Graining Applications (VOTCA) package[62–64] was employed for both the derivation of tabulated potentials

and the analysis of CG trajectories. Since often coarse–grained systems have higher pressures than the atomistic counterparts at the same density,[35] we set the number densities of chains in the coarse–grained models to be the same as those of corresponding atomistic systems, as shown in Table 1. The generated potentials are applied to larger CG systems by replicating the original box in all 3 periodic dimensions and keeping the number densities constant for each concentration (in CG–LB, the box lengths were replicated to within one LB grid spacing, of length $\frac{1}{3}$ nm). Thus, possible size effects on the RDFs should be largely eliminated.

The CG simulation boxes were composed of 24 chains of 20 beads with the box size taken as the average box from the reference simulation at 305 K and the corresponding concentration. The 67.7 %wt system with 1:3 molar concentration of monomers in water acquired linear dimension of 40 Å, 44 %wt − 46.3 Å, and 50.9 Å for the 33.5 %wt system, respectively. The starting configuration was chosen as the mapped last snapshot of the corresponding parent AA–MD simulation after at least 200 ns of simulation. The bond and angle probability distributions sampled during the AA–MD simulations were Boltzmann inverted to the tabulated bonded potential (see supporting information) using Eq. 3, excluding all contributions due to terminal backbone beads B. Initial CG pair potentials for use in IBI iterations were generated from reference RDFs, $g^{ij}_{ref}(r)$, according to Eq. 4. Different starting potentials can be useful, in particular for situations where the iterative procedure may be unstable because intermediate CG models lead to phase separation. All optimization procedures started with the PMF potential at the corresponding concentration. If the IBI–iteration did not converge (in the 33.5 %wt case), we started from the best (converged) potential at a higher concentration (44 %wt).

All consecutive IBI iterations without any additional constraints were performed using the same protocol: the initial configuration was equilibrated with a Langevin thermostat at 305 K for 0.5 ns followed by a 2 ns simulation using a Nosé–Hoover thermostat, during which RDFs with excluded 1–4 interactions were sampled every 1 ps. The integration time step

was 2 fs and the cutoff distance for non–bonded interactions 18 Å. Every iteration step one of three non–bonded potentials in turn was updated according to Eq. 5. The final, converged CG potential was used to run an extended CG–MD simulations with 192 decamers for a total of $5 \times 10^7$ steps, from which average bond and angle distributions and RDFs were assessed over the last $5 \times 10^6$ steps.

## Coupling to Lattice–Boltzmann Hydrodynamics

All coarse–grained combined polymer Lattice–Boltzmann simulations were performed using the MD suite ESPResSo version 3.2.0, development code version 678-g31c4458.[65] The hydrodynamic interactions were computed using the Lattice–Boltzmann (LB) method implemented on GPUs.[44] Each simulation was performed on the Surface machine at Lawrence Livermore National Laboratory on sixteen Intel Xeon E5-2670 processors and one NVIDIA Tesla K40m GPU.

In the coarse–grained Lattice–Boltzmann (CG–LB) ESPResSo studies, a unit system for the NIPAM high density polymer phase was established: $M_0 = 50$ amu, $\sigma = \frac{1}{3}$ nm, $\epsilon = k_B 305$ K, $t_0 = \sigma\sqrt{\epsilon/M_0} = 1.4799$ ps. The input parameters to LB are bead resistance (input friction) constant $\xi_{bead}$ (eq. 1), fluid density $\rho$, lattice spacing $a_{grid}$, kinematic fluid viscosity $\nu$ and the fluid time step $\Delta t_{LB}$. Simulations were carried out at 290, 305, and 320 K, and the density and kinematic viscosity of water at these temperatures were taken from IAPWS 2008.[66] The properties of water are listed in Table 2. The LB grid spacing is $\frac{1}{3}$ nm, which is approximately the distance between MD beads. Replicating the box in 3 dimensions (see above) eliminates size effects that would result in an unusually small grid of 12 nodes along one dimension.

**Table 2: Properties of water and their effects on simulation parameters**

| T [K] | $\rho$ $[M_0/\sigma^3]$ | $\eta$ $[\sigma^2/t_0]$ | speed–up factor | MD time step [fs] | trajectory length [ns] |
|---|---|---|---|---|---|
| 290 | 0.4455 | 14.40 | 18.00 | 26.64 | 1333 |
| 305 | 0.4438 | 10.23 | 12.79 | 18.93 | 946.4 |
| 320 | 0.4413 | 7.74 | 9.68 | 14.33 | 716.3 |

In simulation units, the kinematic viscosity for the three selected temperatures are 14.398, 10.232, 7.744 $\sigma^2/t_0$. We scale the kinematic viscosity to 0.8 as it increases the effective time step by a factor of $\eta/0.8$. The time step was therefore indirectly dependent on temperature.

In order to match the slow dynamics of the all–atom simulations, we used input friction (Eq. 1) values near the limit of the allowable values for a given time step. Smaller time steps allow higher friction values. For a time step of $dt = 0.01\ t_0 = 189$ fs, the friction used was $1.683 \times 10^{-11}$ kg/s and for a time step of $0.001\ t_0 = 18.9$ fs it was $2.244 \times 10^{-10}$ kg/s. The lower friction value $1.683 \times 10^{-11}$ was also used for $dt = 18.9$ fs to compare the effects of time step on CG molecular structure. The LB fluid positions and velocities were updated every four MD integration steps.

The bonded and nonbonded potentials calculated by IBI were transferred to ESPResSo in order for the hydrodynamics of the system to be simulated using the LB method. The starting configuration for the CG–LB simulations was taken from a mapped snapshot of the equilibrated AA system. The CG–LB system was first equilibrated with forces capped at values that were increased linearly for 50 cycles of 100 steps of step size $0.001\ t_0$ in LB fluid at $T = 30.5$ K with $\xi = 5.610 \times 10^{-14}$ kg/s. The force cap was then removed and $T$, and friction $\xi$, and the time step were adjusted to the production run values. Once the particles were warmed to the correct kinetic energy the production run measurements began.

CG bead positions were recorded every $10t_0$. For the $T = 305$ K, 44 %wt and 67 %wt systems, CG bead positions were recorded every 25 steps in order to obtain high resolution short lag time dynamical information. 5000 snapshots were recorded in each simulation, resulting in simulations lengths of 1331.8, 946.4, and 716.3 ns for the 290, 305, and 320 K systems, respectively. The velocity of the center of mass of the system was reset every $10^4$ steps. The bond distributions and radial distribution functions were measured using VOTCA[62–64] for comparison to the AA system. Details of the CG–LB simulations are in Table 1.

Static and dynamic analysis of these systems was performed post–simulation. The mean

squared displacement, autocorrelation function of the polymer end–to–end vector of all 192 decamers, and autocorrelation functions of certain A–B–B–A dihedrals were determined for AA, CG–MD and CG–LB systems. The mean squared displacement (MSD) of the chains provides hydrodynamic information at short times and diffusion coefficients at long times. The position of the fifth monomer along each decamer was used for the mean squared displacement. The mean squared displacement was calculated by

$$MSD = \left\langle (\overline{r}(t) - \overline{r}(t+\tau))^2 \right\rangle_1 \tag{7}$$

where $\overline{r}(t)$ is the position of the point of interest (here monomer 5) at time $t$ and $\overline{r}(t+\tau)$ is the position of the same point along the chain at a later time $t+\tau$. A system–wide MSD was calculated by taking the arithmetic mean of the MSD of all decamers; the operator $\langle a \rangle_1$ takes the mean value of $a$ over all origin times $t$ and all chains in the system.

The end–to–end vector $\overline{e} = \overline{r}_{10}(t) - \overline{r}_1(t)$ of each decamer was determined at each time point and the autocorrelation function of the end to end vector was determined by

$$ACF = \left\langle (\hat{e}(t) - \hat{e}(t+\tau))^2 \right\rangle_1 \tag{8}$$

where $\hat{e}(t)$ is the unit end–to–end vector of one polymer at time $t$ and $\hat{e}(t+\tau)$ is the position of the same end–to–end vector at a later time $t+\tau$. In the AA system, the coordinates of the first backbone carbon with a side group and the tenth and final backbone carbon with a side group were used to define the end–to–end vector of the polymer. In the CG–MD and CG–LB systems, the first and tenth backbone (B) beads were used to define the end–to–end vector.

In the dihedral analysis, the A–B–B–A dihedral angles of the middle seven dyads of chains $1-8$ were recorded and analyzed by:

$$C(\tau) = \langle (cos[\Theta(t) - \Theta(t+\tau)] \rangle_2 \, . \tag{9}$$

Since chains $1-8$ have the same stereochemistry, the data for each backbone dyad torsional angle can be averaged. This is represented by the operator $\langle a \rangle_2$ that takes the mean value of $a$ over all origin times $t$ and all chains $1-8$. The other groups of chains in the system, $9-16$ and $17-24$ have similar behavior and are not shown.

# Results and Discussion

We first present the development of a CG model of NIPAM with implicit solvent using the IBI method and then combine the resulting model with the LB fluid model.

## Intra–Molecular Structure

The intramolecular bonding structure of the CG systems was compared to the AA system. The potentials for CG bonds were created directly from the bond distributions of the CG beads mapped on to the all–atom system and the resulting distributions in the CG simulation correspond closely to the parent simulation. The bond distributions for B–B and A–B bonds as well as B–B–B and A–B–B angles were determined from 5000 snapshots. The results for the 44 %wt system are provided in Figure 2.

The CG bond structure contains multiple peaks and shoulders. These are the result of atomistic dihedral rotations mapping onto CG bonds and angles; tacticity was averaged over. The features in the CG bond structure represent multiple atomistic states.

There are two peaks in the distribution of the B–B backbone–backbone bond: a main peak at $r = 3.25$ Å and a minor peak at $r = 3.70$ Å (Figure 2(a)). These features are represented in all simulations, but the relative proportions are different. The CG–MD system closely follows the AA–MD distribution. The CG–LB simulation with low input friction and $dt = 18.9$ fs has a slightly weaker major peak and slightly boosted minor peak. These differences are increasingly pronounced for CG–LB with high input friction, $dt = 18.9$ fs, and CG–LB with low input friction, $dt = 189$ fs. The latter two distributions are also

characterized by a broadening of the peaks.

There is a peak and a shoulder in the distribution of the A–B sidechain–backbone bond: a peak at $r = 3.45$ Å and a shoulder near $r = 3.25$ Å(Figure 2(c)). The CG–MD and CG–LB, low friction, $dt = 18.9$ fs both show close agreement with the AA system. The CG–LB, high friction, $dt = 18.9$ fs and CG–LB, low friction, $dt = 189$ fs systems show a decreased major peak and boosted shoulder and broadening compared to the AA system.

There is one peak and four shoulders in the distribution of the B–B–B (backbone) angle: the peak is at $\Theta = 1.91$ with shoulders near $\Theta = 1.30$, $\Theta = 1.63$, $\Theta = 2.05$, and $\Theta = 2.42$ (Figure 2(b)). For all CG systems, the small angle shoulders are diminished, the large angle shoulders are boosted, and the peak is shifted to larger $\Theta = 1.93$.

There is one peak and one pronounced shoulder in the distribution of the A–B–B sidechain–backbone–backbone angle bond: the maximum peak is at $\Theta = 1.91$ and the shoulder is near $\Theta = 2.64$ (Figure 2(d)). For all CG systems, the peak was shifted to $\Theta = 1.95$.

We investigated the autocorrelation function of the A–B–B–A dihedral angles in order to determine if tacticity was preserved between the AA and CG systems (see Supporting Information). The ACF is a dynamical property, but its result supports the static structure property of tacticity. The dihedral autocorrelation function was defined by Eq. 9. Each curve corresponds to one dyad, and eight chains were included in each autocorrelation function. The long–time values of the autocorrelation functions for the AA system are positive and therefore the chains in the AA system maintain tacticity.[67] The autocorrelation functions in the CG–LB system decay to zero, suggesting the A–B–B–A dihedral angles are uncorrelated at long times and do not maintain tacticity.

## Non–bonded pair potentials

In Figure 3 we show the evolution of non–bonded distributions of the CG-beads during IBI optimization. These distribution functions are based on the analysis of configurations from IBI iterations at 67.7 %wt or 44 %wt concentrations and $T = 305$ K. Since all 3 non–bonded

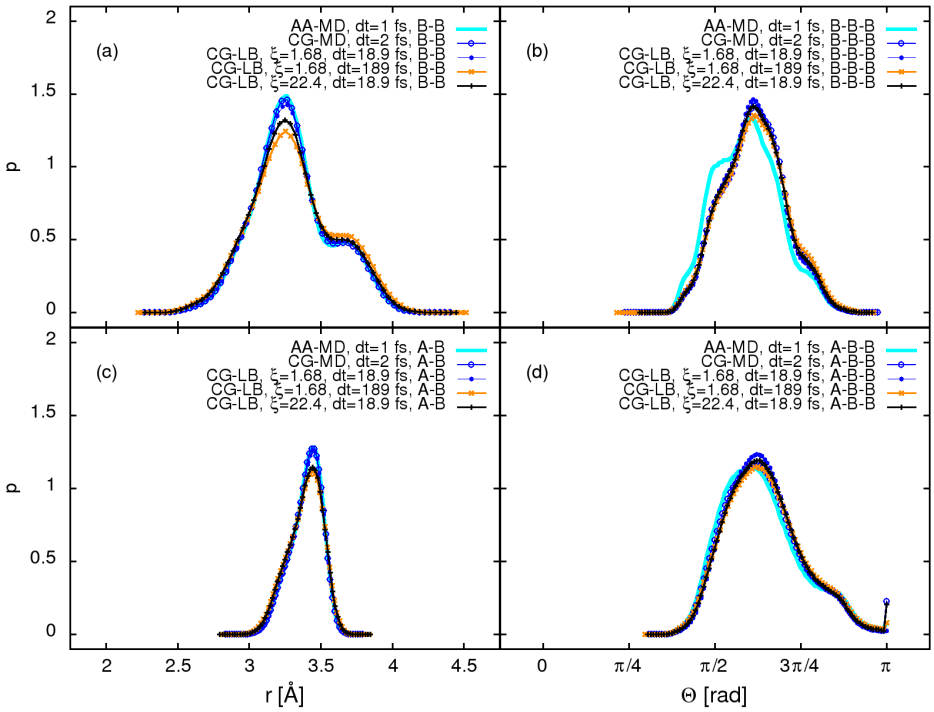


Figure 2: Bond distributions of 44 %wt polymer mixtures for AA–MD, CG–MD and CG–LB systems. (a): B–B bond distribution, (b): B–B–B angle distribution, (c): A–B bond distribution (d): A–B–B angle distribution. Distributions are normalized with respect to the Jacobians: $r^2$ and $\sin\theta$ for linear bonds and angles, respectively. $\Theta = \pi$ refers to a fully extended angle. Black: AA–MD distribution; cyan: CG–MD distribution; blue: CG–LB, low friction, $dt = 189$ fs system; green: CG–LB, low friction, $dt = 18.9$ fs system; grey: CG–LB, high friction, $dt = 18.9$ fs system. The units for LB bead resistance $\xi_{bead}$ are $10^{-11}$ $kg/s$. The B–B bond distributions have been scaled by 0.8, and the A–B bond distributions have been scaled by 0.333.

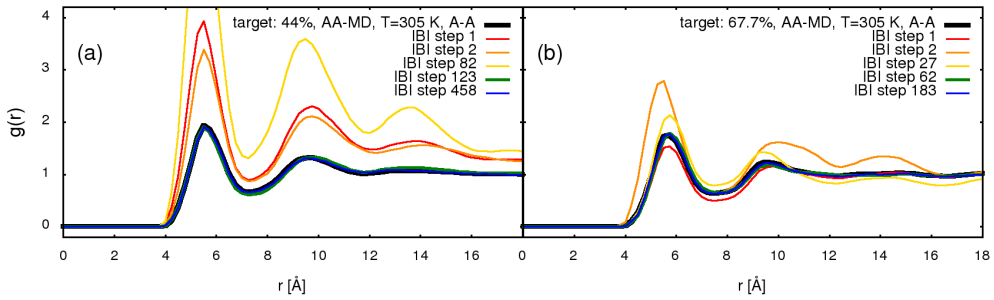


Figure 3: Radial distribution functions of CG beads during IBI optimization. a: A–A in 44 %wt polymer system. b: A–A in 67.7 %wt polymer system. The IBI results displayed correspond to the following iterative steps: 44 %wt (a): black line: target atomistic radial distribution function, red line: step 1, orange line: step 2, yellow line: step 82, green line: step 123, blue line: step 458. 67 %wt (b): black line: target atomistic radial distribution function, red line: step 1, orange line: step 2, yellow line: step 27, green line: step 62, blue line: step 183. A–B and B–B nonbonded correlations are found in the SI.

distributions (A–A, B–B and A–B) show similar features, we discuss here the A–A RDF only and the rest is provided in Supporting Information. The A–A RDF reveals multiple peaks with the first peak centered at 5.5 Å in the reference RDF and in the consecutive refinements due to IBI updates to the pair potential, although the height of the peak varies significantly owing to the intra–molecular contributions to the non–uniform density. Figure 3 also shows that the IBI convergence significantly varies with concentration: at 67.7 %wt the relative error between CG and target A–A RDF is below 3 % after 183 iterations and reasonable accuracy is achieved already after 60 iterations, while at 44 %wt the same level of accuracy is achieved only after 450 iterations. In the reference atomistic RDF with decreasing the concentration from 67.7 %wt to 44 %wt, the first peaks of the A–A RDF increases in height by 10 % and narrows slightly, which indicates the rise of intra–molecular correlations (contributions due to 1–5 neighbors) and overall inhomogeneity of the system. This change in convergence speed becomes even more severe with further decrease of concentration: at 33.5 %wt no converged potential was found after 500 iterations with relative error growing with the number of iterations. One rational way to improve the overall stability of IBI procedure and the speed of convergence of the method is to rely on a high quality initial guess of the potential to refine. As starting point we used the converged potential of 44 %wt

system with mixing parameter $\alpha$ set to 0.3, but the same divergent behavior was observed in all 3 IBI potentials, showing the limits of the straightforward IBI approach in implicit solvent systems. Since the exact cause of the IBI failure at lower concentrations remains unclear, we do not provide the results of IBI optimization at 33.5 %wt.

The accuracy of the nonbonded parameters in the PNIPAM CG model was assessed by comparing RDFs from the atomistic simulations of 24 decamers and CG simulations with 192 decamers at 44.0 %wt and 67.7 %wt of NIPAM, respectively, at T= 305 K. Figure 4 compares the A–A RDFs of the AA, CG–MD, and CG–LB trajectories at those state points. Besides small differences in the A–B distribution in the 44 %wt system, the CG–LB nonbonded statistics follow the CG–MD system closely and match the target distributions arguably well. This indicates that the calculated CG potentials reproduce the structural features of high to moderate PNIPAM solutions at CG level. A–B and B–B non–bonded correlations are found in the SI.

Figure 5 shows the RDF of A–A beads based on the CG–LB time step and friction. A–B and B–B nonbonded correlations are found in the SI. Parameters tested in CG–LB were time step: $dt$ = 18.9 and 189 fs, and friction: $1.683 \times 10^{-11}$ and $2.244 \times 10^{-10}$ kg/s. The lower friction value with the 18.9 fs time step provided the closest agreement in the nonbonded structure with respect to the AA system. The peak heights in the high friction value with 18.9 fs time step were depressed with respect to the AA system. This depression of the RDF was more pronounced in the simulation with lower friction and 189 fs time step. This shows that low friction values, create smaller forces between the CG–MD beads and the LB fluid which preserves the structure more accurately than high friction values. High friction values may be necessary to match the dynamics to AA systems, however. Larger time steps also lead the system to experience forces further from the minima in the force fields and thus may be less accurate due to weaker sampling. A near 10–fold time step with respect to atomistic dynamics was accomplished, while also replacing the explicit solvent with LB.

Having validated the approach for one state point, we now want to test if the same po-

tentials can be used for a wider range of state points. In using the non–bonded potentials derived above in our PNIPAM CG model, we consider two factors: (i) temperature transferability of the potentials derived at 305 K to 290 K and 320 K, and (ii) concentration transferability of the potentials derived at 44 %wt to 67.7 %wt and 33.5 %wt. Bonded potentials are much stronger compared to thermal energy that these changes in condition have negligible effects. Figure 6 compares the A–A results when the potential developed at 305 K and 44 %wt was transferred to T=290 K or T=320 K. There are only weak temperature effects in the AA system with increased height of the first peak by about 10 % at 320 K and the CG potential results follow this behavior. Figure 7 compares the A–A results when the potential developed at 305 K and 67.7 %wt was transferred to T=290 K and T=320 K. A–B and B–B nonbonded correlations are found in the SI.

Figure 8 compares the A–A results when the potential developed at 44 %wt was transferred to 67.7 %wt and 33.5 %wt. We clearly see a much stronger effect with concentration than with temperature. The A–A (here) and A–B (SI) interactions are qualitatively the same over all concentrations. But the B–B (SI) does not transfer correctly as the initial shoulder comes in too low. Also the shape of the first peak is not reproduced correctly. The developed potentials demonstrate notable concentration dependence. However, it is promising that all sets of derived potentials – based on an implicit solvent model – provided acceptable transferability over the temperature range of 290–320 K. Noteworthy, the best agreement with target distributions was achieved with potentials based on reference atomistic system having monomer:water concentration of 1:3, which almost corresponds to a polymer melt. This observation indicates that IBI CG models favorably reproduce the structural properties of homogeneous stems such as polymer melts, but are less successful to describe systems with density or concentration heterogeneities.

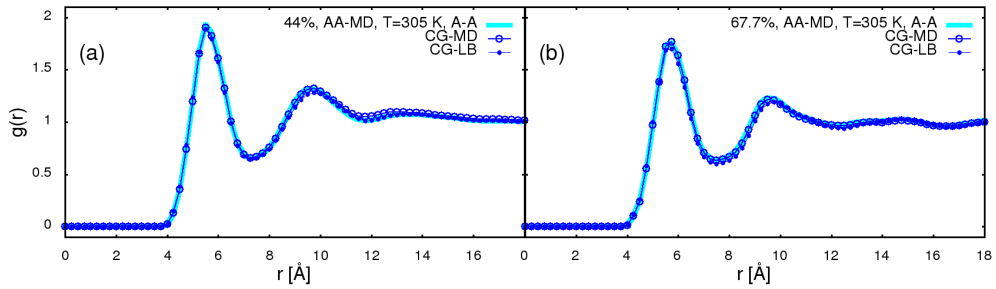


Figure 4: Radial distribution function $g(r)$ between different bead types in AA, CG–MD, and CG–LB systems at $T = 305$ K. The CG simulations are performed with the potentials obtained from a converged IBI procedure at $T = 305$ K. Cyan line: AA target potential. Blue hollow circle: CG–MD simulation. Blue filled circle: CG–LB, low friction, $dt = 18.9$ ps simulation. (a): A–A distribution in 44 %wt polymer-water mixture. (b): A–A distribution in 67.7 %wt polymer-water mixture. A–B and B–B correlations are found in the SI.

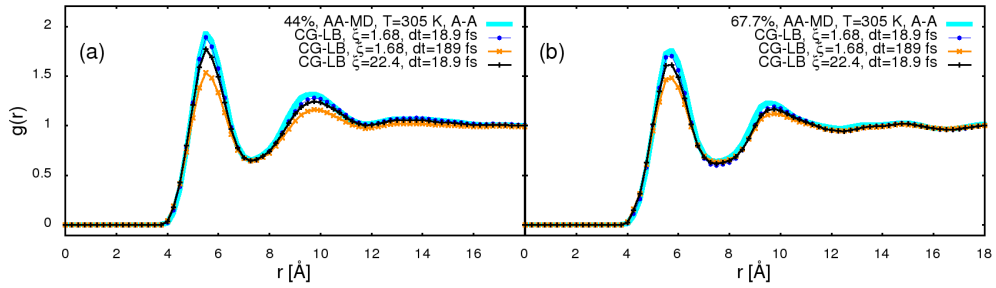


Figure 5: Radial distribution function $g(r)$ between different bead types comparing the target AA system to CG–LB systems with various time steps and input frictions. In each panel, all curves represent the same concentration, temperature, and bead pair correlation. Cyan line: AA target potential. Blue filled circle: CG–LB, low friction, $dt = 18.9$ ps simulation. Orange x: CG–LB, low friction, $dt = 189$ ps. Black +: CG–LB, high friction, dt=18.9 ps. (a): A–A distribution in 44 %wt polymer-water mixture. (b): A–A distribution in 67.7 %wt polymer-water mixture. A–B and B–B correlations are found in the SI. The units for LB bead resistance $\xi_{bead}$ are $10^{-11}$ $kg/s$.

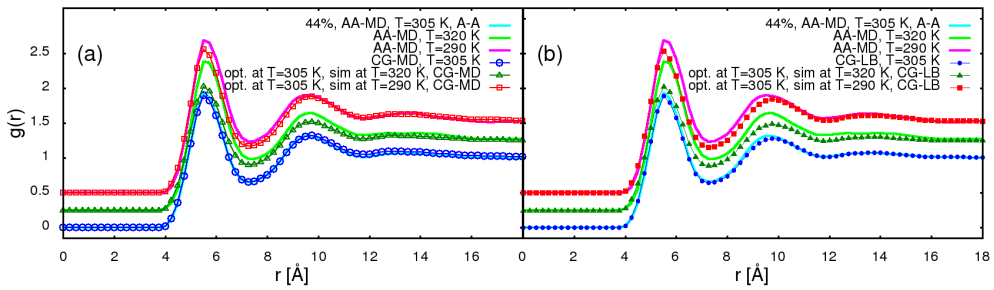


Figure 6: Radial distribution function $g(r)$ between different bead types in AA, CG–MD, and CG–LB systems. The CG simulations are simulated with an IBI potential optimized from AA–MD trajectories at 44 %wt concentration and $T = 305$ K and were transferred to different temperatures. In each panel, all curves represent the same concentration and bead pair correlation. Cyan line: AA target potential at $T = 305$ K. Fuchsia line: AA at $T = 290$ K. Lime green line: AA at $T = 320$ K. Blue hollow circle: CG–MD at T=305 K. Red hollow square: CG–MD at $T = 290$ K. Green hollow triangle: CG–MD at $T = 320$ K. Blue filled circle: CG–LB at $T = 305$ K. Red filled square: CG–LB at $T = 290$ K. Green filled triangle: CG–LB at $T = 320$ K. All CG–LB results in this figure are based on low friction, $dt = 18.9$ ps simulations. (a): A–A distribution in CG–MD simulation. (b): A–A distribution in CG–LB simulation. Curves for $T = 290$ K are offset by +0.5, and curves for $T = 320$ K are offset by +0.25. A–B and B–B correlations are found in the SI. The units for LB bead resistance $\xi_{bead}$ are $10^{-11}$ $kg/s$.

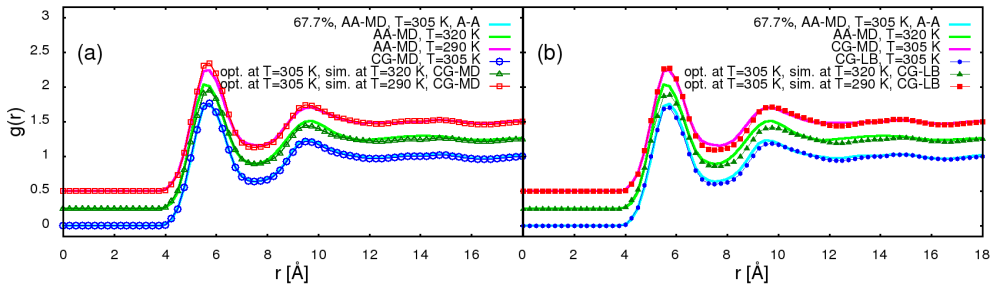


Figure 7: Radial distribution function $g(r)$ between different bead types in AA, CG–MD, and CG–LB systems. The CG simulations are simulated with an IBI potential optimized from AA–MD trajectories at 67.7 %wt concentration and T=305 K and were transferred to different temperatures. In each panel, all curves represent the same concentration and bead pair correlation. Cyan line: AA target potential at $T = 305$ K. Fuchsia line: AA at $T = 290$ K. Lime green line: AA at $T = 320$ K. Blue hollow circle: CG–MD at $T = 305$ K. Red hollow square: CG–MD at $T = 290$ K. Green hollow triangle: CG–MD at $T = 320$ K. Blue filled circle: CG–LB at $T = 305$ K. Red filled square: CG–LB at $T = 290$ K. Green filled triangle: CG–LB at $T = 320$ K. All CG–LB results in this figure are based on low friction, $dt = 18.9$ ps simulations. (a): A–A distribution in CG–MD simulation. (b): A–A distribution in CG–LB simulation. Curves for $T = 290$ K are offset by +0.5, and curves for $T = 320$ K are offset by +0.25. A–B and B–B correlations are found in the SI. The units for LB bead resistance $\xi_{bead}$ are $10^{-11}$ $kg/s$.

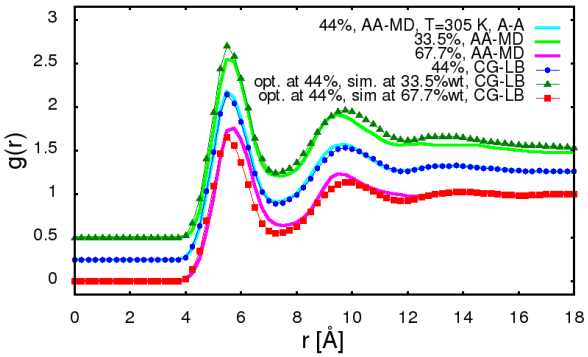


Figure 8: Radial distribution function $g(r)$ between different bead types in AA, CG–MD, and CG–LB systems. The CG simulations are simulated with an IBI potential optimized from AA–MD trajectories at 44 %wt concentration and $T = 305$ K and were transferred to different concentrations. In each panel, all curves represent the same temperature and bead pair correlation. Cyan line: AA target potential at 44 %wt. Fuchsia line: AA at 67.7 %wt. Lime green line: AA at 33.5 %wt. Blue filled circle: CG–LB at 44 %wt. Red filled square: CG–LB at 67.7 %wt. Green filled triangle: CG–LB at 33.5 %wt. All CG–LB results in this figure are based on low friction, $dt = 18.9$ ps simulations. (a): A–A distribution in CG–MD simulation. (b): A–A distribution in CG–LB simulation. Curves for 33.5 %wt are offset by +0.5, and curves for 44 %wt are offset by +0.25. A–B and B–B correlations are found in the SI. The units for LB bead resistance $\xi_{bead}$ are $10^{-11}$ $kg/s$.

## Dynamics

In addition to the reproduction of structural properties, the combined CG–LB model should be capable to account for certain dynamic effects of the reference system. The dynamics of the all–atom and coarse–grained lattice Boltzmann systems were validated by analyzing the mean squared displacement and autocorrelation function of the end to end vector of the decamers.

The slope of the MSD *versus* time lag $\tau$ on a log–log plot is indicative of the dynamic state of the system. The Zimm model[68] accounts for hydrodynamic interactions between beads on the polymer chain while calculating the pre–averaged mobility matrix. Zimm dynamics is characterized by monomer MSD$\propto \tau^{2/3}$ at short times followed by MSD$\propto \tau^{1}$ beyond the Zimm time, or the relaxation time of the polymer. The MSD of the center of mass for decamers for the all–atom 44 %wt system is shown in Figure 9. The all–atom system (blue line) exhibits $\propto \tau^{2/3} \rightarrow \propto \tau^{1}$ behavior, in agreement with Zimm behavior. The CG–MD

(green line) and CG–LB systems (low friction, purple line; high friction, red line) exhibit $\propto \tau^2 \rightarrow \propto \tau^1$ time scaling behavior. It is possible that the coarse–grained system does not have polymer scaling behavior at these short chain lengths due to the reduced number of interaction sites. We are currently studying longer chains which give an indication of Zimm behavior. The LB friction on the MD beads $\xi_{bead}$ decreased the values and slopes of the MSD as the friction increased, but the dynamical transition times are similar, as shown in Figure 9.

The diffusion coefficient is related to the slope of the MSD in the linear regime, for lag times greater than the longest relaxation time of the chains, by

$$D_t = \lim_{\tau \to \infty} \frac{MSD}{2d\tau} = \lim_{\tau \to \infty} \frac{\langle (\overline{r}(t) - \overline{r}(t+\tau))^2 \rangle}{6\tau} \tag{10}$$

where $d$ is the number of spatial dimensions. The diffusion coefficients were calculated from a least squares fit of the slopes of the MSDs and are listed in Table 3. The closest match to the AA system is the high friction CG–LB simulation. Even with a friction value so large that the static behavior is not fully reproduced, $2.244 \times 10^{-12}$ kg/s, for the 18.9 fs timestep the diffusion coefficient is larger than the AA system by a factor of 4.2.

The MSD of the central monomers of decamers for the AA–MD 67 %wt system is provided in Figure 10. The dynamics is quite slow for this system. At 100 ns, the MSD of the central monomers of the chains is 10 $\text{Å}^2$. The MSD scales as $\propto \tau^{1/4}$ followed by $\propto \tau^{1/2}$ and eventually free diffusion at $\propto \tau^1$, suggestive of a slowdown similar to reptation dynamics.[69] It would be surprising to truly observe reptation dynamics at this chain length. The enhanced interactions between the polymer and water atoms, $k_{ij} = 1.35$, clearly played a role in the slow dynamics, however, it is unclear if the MSD *versus* $\tau$ scaling was also affected. The atoms may have been trapped due to the stronger interactions, particularly the hydrogen bonds. This is in agreement with our earlier atomistic observation that a weaker interaction of the unpolar groups with water leads to more glass–like behavior and slower dynamics.[29] In the CG simulations, the direct interaction with water is missing and replaced with a mean–

field type interaction. The CG–LB MSD data is also provided in Figure 10. The CG–LB data follows the trends of the lower concentration system in terms of scaling regimes and friction.

The end–to–end vector autocorrelation functions of the decamers were fit to the Kohlrausch-Williams-Watts[70] (KWW) stretched exponential function:

$$f(t) = Ze^{(t/\tau_{KWW})^{\beta}} \tag{11}$$

where $\tau_{KWW}$ is the relaxation time, $\beta$ is the stretching exponent between 0 and 1, and $Z$ is a constant. The KWW function is useful for describing a curve as the superposition of multiple exponential functions with distinct relaxation times. The average lengths of the end–to–end vectors are in the CG model (CG–MD: $14.32 \pm 0.02$ Å, CG–LB: $15.19 \pm 0.01$ Å) actually slightly smaller than in the AA model ($17.36 \pm 0.12$ Å), there is no significant tacticity effect in the AA model.

As the distribution of relaxation times broadens, $\beta$ decreases. The fit is described in Table 3. The $\beta$ values for the three CG systems agree very well, but the $\beta$ value for the AA system is lower than the CG systems by about 0.3 indicating a wider distribution of correlation times. The AA decamer has 19 carbon–carbon bonds along the backbone, whereas the CG decamer has 9 B–B bonds and significantly fewer degrees of freedom. The data therefore agrees with this concept of a distribution of narrower relaxation times. To probe any mapping effects on end–to–end vector autocorrelation, the end–to–end vector of the decamers with CG beads mapped onto the AA decamers during the AA simulation were also recorded along with the true AA decamer end–to–end vector. The autocorrelation CG–mapped AA data and true AA data were identical.

The longest relaxation time $\tau_R$ of the chains was determined where the autocorrelation function was linear on a semilog plot. This is the decay time of the entire chain. These times are given in Table 3.

The decay time of the CG–LB systems depends on the input friction, and the speedup

**Table 3: Diffusion coefficients and reorientation fit parameters for the 44 %wt system. The units for LB bead resistance $\xi_{bead}$ are $10^{-11}$ $kg/s$.**

| System representation | D [$10^{-7}$cm$^2$/s] | Z | $\beta$ | $\tau_{KWW}$ [ns] | $\tau_R$ [ns] |
|---|---|---|---|---|---|
| AA–MD | 0.6740 | 0.96 | 0.54 | 67.09 | 95.61 |
| CG–MD | 52.09 | 1.01 | 0.83 | 0.02076 | 0.03480 |
| CG–LB $\xi_{bead}$=1.68 | 5.469 | 0.99 | 0.81 | 1.611 | 2.458 |
| CG–LB $\xi_{bead}$=22.4 | 2.848 | 0.99 | 0.81 | 3.482 | 5.234 |

from CG–LB to AA was 20.36 and 43.40, respectively. The speedup in reorientation of the CG–MD system compared to the AA system yielded a factor of 3065. The end–to–end ACF of the decamers in the 44 %wt systems are shown in Figure 11. In this plot, the CG systems were scaled by the ratio between the decay time of the AA system and the respective CG system. The AA system approaches the linear regime in the semilogarithmic plot at larger values of the ACF compared with the CG systems. In the plot, this appears as a steep initial drop, and reflects the faster initial relaxation times not present in the CG systems. This is due to the CG model only representing the long time dynamics of the whole chain or significant subchains and not the fast segmental dynamics. But the long time dynamics is represented semi–quantitatively. The KWW and largest relaxation time fits are provided in the SI.

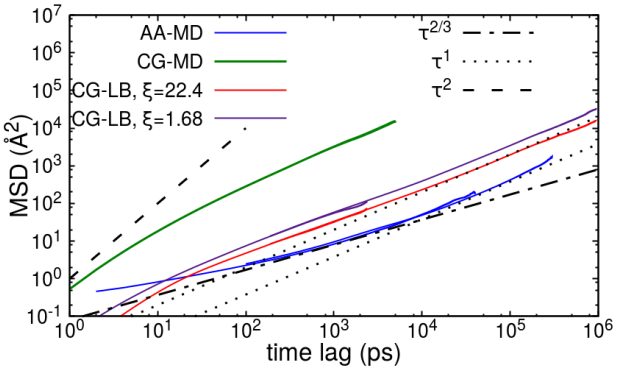


Figure 9: Mean squared displacement of middle monomers in all–atom and coarse–grained lattice Boltzmann 44 %wt polymer–water mixture. Two $\tau^1$ curves are drawn to guide the eye to diffusive regimes of multiple systems. Each AA–MD and each CG–LB MSD curve is an overlay of a high resolution (small $\tau$ between output frames) and a low resolution (large $\tau$ between output frames) trajectory. The overlay begins smooth but discrepancies increase as the statistics of the high resolution trajectory become poor.

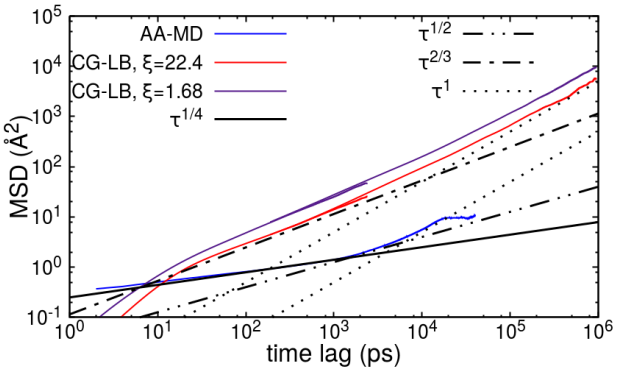


Figure 10: Mean squared displacement of middle monomers in all–atom and coarse–grained lattice Boltzmann 67 %wt polymer–water mixture. Two $\tau^1$ curves are drawn to guide the eye to diffusive regimes of multiple systems. Each AA–MD and each CG–LB MSD curve is an overlay of a high resolution (small $\tau$) and a low resolution (large $\tau$) trajectory. The overlay begins smooth but discrepancies increase as the statistics of the high resolution trajectory become poor.

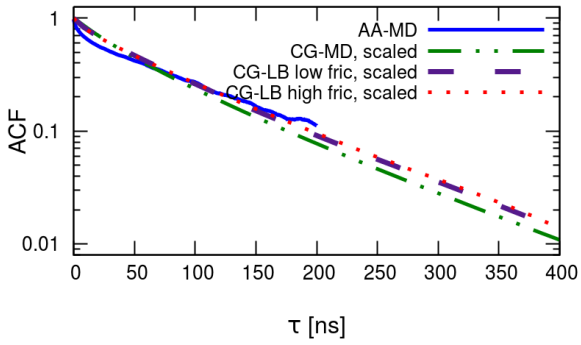


Figure 11: Polymer end to end vector autocorrelation function for AA–MD, CG–MD, and CG–NH systems.

# Conclusion

We have successfully coarse–grained a system of atactic NIPAM using the Boltzmann inversion technique. The two state points for coarse-graining were 44 %wt and 67.7 %wt in water at $T = 305$ K. The nonbonded interactions were calculated using IBI, and the bonded interactions were calculated *via* a single Boltzmann inversion. These two potentials were coupled to an LB fluid, marking the first time a structurally coarse–grained chemical has been coupled to LB. The static properties of the system were preserved in the transfer from an all-atom system to a coarse–grained system with Nose–Hoover thermostat and barostat to the coarse-grained system coupled to LB. Time steps as high as 189 fs were possible in the CG-LB system. The speedup was accomplished through a combination of softer potentials plus a relaxation of the fluid which has a time scaling effect. The potential may be extended by considering tacticity when analyzing bond lengths, angles, and dihedrals. That would increase the workload somewhat as the different dyads would need to be analyzed separately.

The purpose of the LB fluid in these simulations was to replace explicit water with a fast hydrodynamic solver. To the issue of speed, simulation times of 200 $\mu$s per day were accomplished on sixteen CPU cores plus one GPU, the latter of which handled the LB computation. To the matter of hydrodynamics, the polymers were not long enough to see complex polymer behavior such as Zimm, Rouse, or reptation dynamics. We were able to realize a system with diffusivity values of chains within an order of magnitude of the AA system by adjusting the friction to large values relative to the time step. We are currently running simulations at the same state points with longer chains to observe higher order polymer behavior. The tuneable parameter of LB friction modified the magnitude of the dependence on time while preserving the time scaling properties of mean squared displacement and end–to–end vector autocorrelation. Ideally, the friction should be tuned to experimental data to realize exact matching of the dynamical observables between the physical and computational systems. If slow dynamics are desired and high friction values are thus applied the structure may become compromised and due care should be taken. Still

the technique allows a significant speedup with a very good compromise between correct statics and long time dynamics.

## Acknowledgement

The authors thank the Deutsche Forschungsgemeinschaft for support within SFB 985 "Functional microgels and microgel systems" as well as the University of California–National Laboratory Labfee Program (grant number 237353). We also thank the IT center of RWTH Aachen University for providing computational resources under the grant rwth0068 and Lawrence Livermore National Lab for allowing us access to their computer cluster.

## Supporting Information Available

The following files are available free of charge.

- Supplementary.pdf : supplementary data as discussed, radial distribution functions, correlation functions
- state-point-44wt.zip : Optimized potential set at 44 %wt (Lammps format)
- state-point-67wt.zip : Optimized potential set at 67 %wt (Lammps format)
- atomist.zip: Atomistic potential (Lammps format)

## References

(1) Guan, Y.; Zhang, Y. PNIPAM microgels for biomedical applications: from dispersed particles to 3D assemblies. *Soft Matter* **2011**, *7*, 6375–6384.

(2) Schmaljohann, D. Thermo– and pH–responsive polymers in drug delivery. *Advanced Drug Delivery Reviews* **2006**, *58*, 1655–1670.

(3) Ward, M. A.; Georgiou, T. K. Thermoresponsive Polymers for Biomedical Applications. *Polymers* **2011**, *3*, 1215–1242.

(4) de las Heras Alarcon, C.; Pennadam, S.; Alexander, C. Stimuli responsive polymers for biomedical applications. *Chemical Society Reviews* **2005**, *34*, 276–285.

(5) Deshmukh, S.; Mooney, D.; McDermott, T.; Kulkarni, S.; MacElroy, J. D. Molecular modeling of thermo-responsive hydrogels: observation of lower critical solution temperature. *Soft Matter* **2009**, *5*, 1514–1521.

(6) Scherzinger, C.; Schwarz, A.; Bardow, A.; Leonhard, K.; Richtering, W. Cononsolvency of poly-N-isopropyl acrylamide (PNIPAM): Microgels versus linear chains and macrogels. *Current Opinion in Colloid & Interface Science* **2014**, *19*, 84–94.

(7) Kang, Y.; Joo, H.; Kim, J. S. Collapse–Swelling Transitions of a Thermoresponsive, Single Poly(N–isopropylacrylamide) Chain in Water. *J Phys Chem B* **2016**, *120*, 13184–13192.

(8) Lee, S. G.; Pascal, T. A.; Koh, W.; Brunello, G. F.; Goddard, W. A.; Jang, S. S. Deswelling Mechanisms of Surface–Grafted Poly(NIPAAm) Brush: Molecular Dynamics Simulation Approach. *J. Phys. Chem. C* **2012**, *116*, 15974.

(9) Alaghemandi, M.; Spohr, E. Molecular Dynamics Investigation of the Thermo-Responsive Polymer Poly(N–isopropylacrylamide). *Macromol. Theory Simul.* **2012**, *21*, 106.

(10) Adroher-Benitez, I.; Moncho-Jorda, A.; Odriozola, G. Conformation change of an isotactic poly (N–isopropylacrylamide) membrane: Molecular dynamics. *J Chem Phys* **2017**, *146*, 194905.

(11) Wu, C.; Wang, X. Globule-to-Coil Transition of a Single Homopolymer Chain in Solution. *Phys. Rev. Lett.* **1998**, *80*, 4092.

(12) Longhi, G.; Lebon, F.; Abbate, S.; Fornili, S. L. Molecular dynamics simulation of a model oligomer for poly(N–isopropylamide) in water. *Chem. Phys. Lett.* **2004**, *386*, 123.

(13) Walter, J.; Ermatchkov, V.; Vrabec, J.; Hasse, H. Molecular Dynamics and Experimental Study of Conformation Change of Poly(N–isopropylacrylamide) Hydrogels in Water. *Fluid Phase Equilib.* **2010**, *296*, 164.

(14) Du, H.; Wickramasinghe, R.; Qian, X. Effects of Salt on the Lower Critical Solution Temperature of Poly (N–Isopropylacrylamide). *J. Phys. Chem. B* **2010**, *114*, 16594.

(15) Liu, M. S.; Taylor, C.; Chong, B.; Liu, L.; Bilic, A.; Terefe, N. S.; Stockmann, R.; Thang, S. H.; De Silva, K. Conformational Transitions and Dynamics of Thermal Responsive Poly(N–isopropylacrylamide) Polymers as Revealed by Molecular Simulation. *Eur. Polym. J.* **2014**, *55*, 153.

(16) Mayo, S. L.; Olafson, B. D.; Goddard, W. A. DREIDING: a generic force field for molecular simulations. *J Phys Chem* **1990**, *94*, 8897–8909.

(17) Jorgensen, W. L.; Tirado-Rives, J. The OPLS [Optimized Potentials for Liquid Simulations] Potential Functions for Proteins, Energy Minimizations for Crystals of Cyclic Peptides and Crambin. *J. Am. Chem. Soc.* **1988**, *110*, 1657.

(18) Jorgensen, W. L.; Maxwell, D. S.; Tirado-Rives, J. Development and Testing of the OPLS All-Atom Force Field on Conformational Energetics and Properties of Organic Liquids. *J. Am. Chem. Soc.* **1996**, *118*, 11225.

(19) Lukas, D.; Daura, X.; van Gunsteren, W. An Improved GROMOS96 Force Field for Aliphatic Hydrocarbons in the Condensed Phase. *J. Comput. Chem.* **2001**, *22*, 1205.

(20) Oostenbrink, C.; Villa, A.; Mark, A. E.; van Gunsteren, W. F. A Biomolecular Force

Field Based on the Free Enthalpy of Hydration and Solvation: The GROMOS Force-Field Parameter Sets 53A5 and 53A6. *J. Comput. Chem.* **2004**, *25*, 1656.

(21) Cornell, W. D.; Cieplak, P.; Bayly, C. I.; Gould, I. R.; Merz, K. M.; Ferguson, D. M.; Spellmeyer, D. C.; Fox, T.; Caldwell, J. W.; Kollman, P. A. A Second Generation Force Field for the Simulation of Proteins, Nucleic Acids, and Organic Molecules. *J. Am. Chem. Soc.* **1995**, *117*, 5179.

(22) Sun, H.; Mumby, S. J.; Maple, J. R.; Hagler, A. T. An ab Initio CFF93 All–Atom Force Field for Polycarbonates. *J Am Chem Soc* **1994**, *116*, 2978–2987.

(23) Tucker, A. K.; Stevens, M. J. Study of the Polymer Length Dependence of the Single Chain Transition Temperature in Syndiotactic Poly(N–isopropylacrylamide) Oligomers in Water. *Macromolecules* **2012**, *45*, 6697.

(24) Katsumoto, Y.; Kubosaki, N.; Miyata, T. Molecular Approach To Understand the Tacticity Effects on the Hydrophilicity of Poly(N–isopropylacrylamide): Solubility of Dimer Model Compounds in Water. *J. Phys. Chem. B* **2010**, *114*, 13312.

(25) Chiessi, E.; Paradossi, G. Influence of Tacticity on Hydrophobicity of Poly(N–isopropylacrylamide): A Single Chain Molecular Dynamics Simulation Study. *J Phys Chem B* **2016**, *120*, 3765–3776.

(26) de Oliveira, T. E.; Mukherji, D.; Kremer, K.; Netz, P. A. Effects of stereochemistry and copolymerization on the LCST of PNIPAm. *J Chem Physics* **2017**, *146*, 034904.

(27) Deshmukh, S. A.; Sankaranarayanan, S. K. R. S.; Suthar, K.; Mancini, D. C. Role of Solvation Dynamics and Local Ordering of Water in Inducing Conformational Transitions in Poly(N–isopropylacrylamide) Oligomers through the LCST. *J. Phys. Chem. B* **2012**, *116*, 2651.

(28) Abbott, L. J.; Tucker, A. K.; Stevens, M. J. Single Chain Structure of a Poly(N-isopropylacrylamide) Surfactant in Water. *J. Phys. Chem. B* **2015**, *119*, 3837.

(29) Boţan, V.; Ustach, V.; Faller, R.; Leonhard, K. Direct Phase Equilibrium Simulations of NIPAM Oligomers in Water. *J Phys Chem B* **2016**, *120*, 3434–3440.

(30) Wang, Z.; He, X. Developing Coarse-Grained Force Fields for PNIPAM Single Chain from the Atomistic Model. 2009 3rd International Conference on Bioinformatics and Biomedical Engineering. 2009; pp 1–4.

(31) Abbott, L. J.; Stevens, M. J. A temperature–dependent coarse–grained model for the thermoresponsive polymer poly(N–isopropylacrylamide). *J Chem Phys* **2015**, *143*, 244901.

(32) Reith, D.; Pütz, M.; Müller-Plathe, F. Deriving Effective Meso-Scale Coarse Graining Potentials from Atomistic Simulations. *J Comput Chem* **2003**, *24*, 1624–1636.

(33) Sun, Q.; Pon, F.; Faller, R. Multiscale modeling of Polystyrene in various environments. *Fluid Phase Equilibria* **2007**, *261*, 35–40.

(34) Huang, D.; Faller, R.; Do, K.; Moulé, A. Coarse-Grained Computer Simulations of Polymer/Fullerene Bulk Heterojunctions for Organic Photovoltaic Applications. *Journal of Chemical Theory and Computation* **2010**, *6*, 526–537.

(35) Faller, R. Automatic coarse graining of polymers. *Polymer* **2004**, *45*, 3869 – 3876.

(36) Reith, D.; Müller, B.; Müller-Plathe, F.; Wiegand, S. How does the chain extension of poly (acrylic acid) scale in aqueous solution? A combined study with light scattering and computer simulation. *J Chem Phys* **2002**, *116*, 9100–9106.

(37) Faller, R.; Reith, D. Properties of Poly(isoprene): Model Building in the Melt and in Solution. *Macromolecules* **2003**, *36*, 5406–5414.

(38) Dünweg, B.; Ladd, A. J. C. In *Advanced Computer Simulation Approaches for Soft Matter Sciences III*; Holm, C., Kremer, K., Eds.; Springer Berlin Heidelberg: Berlin, Heidelberg, 2009; pp 89–166.

(39) Hoogerbrugge, P. J.; Koelman, J. M. V. A. Simulating Microscopic Hydrodynamic Phenomena with Dissipative Particle Dynamics. *EPL (Europhysics Letters)* **1992**, *19*, 155.

(40) Español, P. Dissipative particle dynamics with energy conservation. *EPL (Europhysics Letters)* **1997**, *40*, 631.

(41) Soddemann, T.; Dünweg, B.; Kremer, K. Dissipative particle dynamics: A useful thermostat for equilibrium and nonequilibrium molecular dynamics simulations. *Phys. Rev. E* **2003**, *68*, 046702.

(42) Gompper, G.; Ihle, T.; Kroll, D.; Winkler, R. In *Advanced Computer Simulation Approaches for Soft Matter Sciences III*; Holm, C., Kremer, K., Eds.; Springer Berlin Heidelberg: Berlin, Heidelberg, 2009; pp 1–87.

(43) Brady, J.; Bossis, G. Stokesian dynamics. *Ann. Rev. Fluid Mech.* **1998**, *20*, 111–157.

(44) Roehm, D.; Arnold, A. Lattice Boltzmann simulations on GPUs with ESPResSo. *Eur. Phys. J. Special Topics* **2012**, *210*, 89–100.

(45) Ahlrichs, P.; Dünweg, B. Simulation of a single polymer chain in solution by combining lattice Boltzmann and molecular dynamics. *J. Chem. Phys.* **1999**, *111*, 8225–8239.

(46) Aidun, C.; Lu, Y.; Ding, E.-J. Direct analysis of particulate suspensions with inertia using the discrete Boltzmann equation. *J. Fluid Mech.* **1998**, *373*, 287–311.

(47) Usta, O.; Ladd, A.; Butler, J. Lattice–Boltzmann simulations of the dynamics of polymer solutions in periodic and confined geometries. *J. Chem. Phys.* **2005**, *122*, 094902.

(48) Jain, A.; Sunthar, P.; Dünweg, B.; Prakash, J. Optimization of a Brownian-dynamics algorithm for semidilute polymer systems. *Phys. Rev. E* **2012**, *85*, 066703.

(49) Mackay, F.; Ollila, S.; Denniston, C. Hydrodynamic forces implemented into LAMMPS through a lattice-Boltzmann fluid. *Comput. Phys. Commun.* **2013**, *184*, 2021–2031.

(50) Plimpton, S. Fast Parallel Algorithms for Short-Range Molecular Dynamics. *J Comp Phys* **1995**, *117*, 1–19.

(51) Brown, W. M.; Wang, P.; Plimpton, S. J.; Tharrington, A. N. Implementing Molecular Dynamics on Hybrid High Performance Computers - Short Range Forces. *Comp Phys Comm* **2011**, *182*, 898–911.

(52) Berendsen, H. J. C.; Grigera, J. R.; Straatsma, T. P. The missing term in effective pair potentials. *J Phys Chem* **1987**, *91*, 6269–6271.

(53) Pamies, R.; Zhu, K. Z.; Kjøniksen, A. L.; Nyström, B. Thermal Response of Low Molecular Weight Poly-(N-isopropylacrylamide) Polymers in Aqueous Solution. *Polym. Bull.* **2009**, *62*, 487.

(54) Duan, Y.; Wu, C.; Chowdhury, S.; Lee, M.; Xiong, G.; Zhang, W.; Yang, R.; Cieplak, P.; Luo, R.; Lee, T. et al. A point-charge force field for molecular mechanics simulations of proteins based on condensed-phase quantum mechanical calculations. *J. Comput. Chem.* **2003**, *24*, 1999–2012.

(55) Ahmed, Z.; Gooding, E. A.; Pimenov, K. V.; Wang, L.; Asher, S. A. UV Resonance Raman Determination of Molecular Mechanism of Poly(N-isopropylacrylamide) Volume Phase Transition. *J Phys Chem B* **2009**, *113*, 4248–4256.

(56) Martinez, L.; Andrade, R.; Birgin, E. G.; Martinez, J. M. Packmol: A package for building initial configurations for molecular dynamics simulations. *Journal of Computational Chemistry* **2009**, *30*, 2157–2164.

(57) Hockney, R.; Eastwood, J. *Computer Simulation Using Particles*; Taylor and Francis: New York, 1988.

(58) Ryckaert, J.-P.; Ciccotti, G.; Berendsen, H. J. Numerical integration of the cartesian equations of motion of a system with constraints: molecular dynamics of n-alkanes. *Journal of Computational Physics* **1977**, *23*, 327 – 341.

(59) Soper, A. Empirical potential Monte Carlo simulation of fluid structure. *Chemical Physics* **1996**, *202*, 295 – 306.

(60) Tschöp, W.; Kremer, K.; Batoulis, J.; Bürger, T.; Hahn, O. Simulation of polymer melts. I. Coarse-graining procedure for polycarbonates. *Acta Polymerica* **1998**, *49*, 61–74.

(61) Ghosh, J.; Faller, R. State point dependence of systematically coarse–grained potentials. *Molecular Simulation* **2007**, *33*, 759–767.

(62) Rühle, V.; Junghans, C.; Lukyanov, A.; Kremer, K.; Andrienko, D. Versatile Object-oriented Toolkit for Coarse-graining Applications. *J. Chem. Theor. Comp.* **2009**, *5*, 3211.

(63) Rühle, V.; Junghans, C. Hybrid approaches to coarse-graining using the VOTCA package: liquid hexane. *Macromol. Theory Simul.* **2011**, *20*, 472.

(64) Mashayak, S.; Jochum, M.; Koschke, K.; Aluru, N.; Rühle, V.; Junghans, C. Relative entropy and optimization-driven coarse-graining methods in VOTCA. *PLoS ONE* **2015**, *10*, e0131754.

(65) Arnold, A.; Lenz, O.; Kesselheim, S.; Weeber, R.; Fahrenberger, F.; Roehm, D.; Košovan, P.; Holm, C. ESPResSo 3.1 — Molecular dynamics software for coarse-grained models. Meshfree Methods for Partial Differential Equations VI. 2013; pp 1–23.

(66) Cooper, J.; Dooley, R. The International Association for the Properties of Water and Steam. Release on the IAPWS Formulation 2008 for the Viscosity of Ordinary Water Substance. 2008; `http://www.iapws.org/relguide/visc.pdf`.

(67) van der Spoel, D.; Berendsen, H. Molecular Dynamics Simulations of Leu-Enkephalin in Water and DMSO. *Biophys J.* **1997**, *72*, 2032–2041.

(68) Zimm, B. Dynamics of polymer molecules in dilute solution: viscoelasticity, flow birefringence and dielectric loss. *J. Chem. Phys.* **1956**, *24*, 269–278.

(69) Doi, M.; Edwards, S. *Theory of Polymer Dynamics*; Wiley: New York, 1987.

(70) Williams, G.; Watts, D. Non–symmetrical dieletric relaxation behavior arising from a simple empirical decay function. *Trans. Faraday Soc.* **1970**, *66*, 80–85.

# Graphical TOC Entry

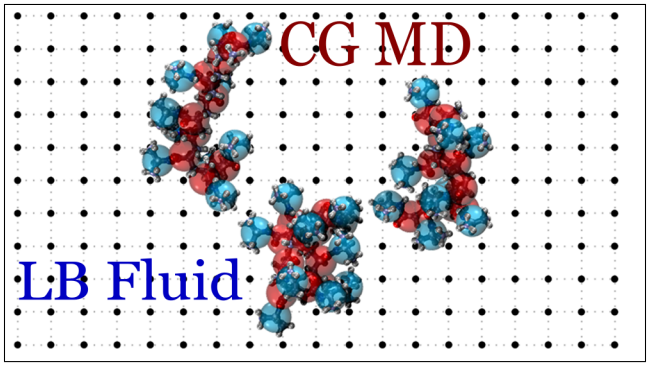


TOC Graphic